Journal of Advanced Ceramics
2023, **12**(4): 830–847
https://doi.org/10.26599/JAC.2023.9220724
ISSN 2226-4108
CN 10-1154/TQ

Research Article

Microstructural tailoring, mechanical and thermal properties of SiC composites fabricated by selective laser sintering and reactive melt infiltration

Xiao Chen[a,b], Jie Yin[a,b,*], Longzhi Huang[a,b], Sea-Hoon Lee[c], Xuejian Liu[a,b,*], Zhengren Huang[a,*]

[a] *State Key Lab of High Performance Ceramics and Superfine Microstructures, Shanghai Institute of Ceramics, Chinese Academy of Sciences, Shanghai 200050, China*
[b] *College of Materials Science and Opto-Electronic Technology, University of Chinese Academy of Sciences, Beijing 100049, China*
[c] *Extreme Materials Institute, Korea Institute of Materials Science, Changwon 51508, Republic of Korea*

Received: October 22, 2022; Revised: January 17, 2023; Accepted: January 19, 2023

Abstract: Poor flowability of printable powders and long preparation cycles are the main challenges in the selective laser sintering (SLS) of chopped carbon fiber (C_f) reinforced silicon carbide (SiC) composites with complex structures. In this study, we develop an efficient and novel processing route in the fabrication of lightweight SiC composites via the SLS of phenolic resin (PR) and C_f powders with the addition of α-SiC particles combined with the one-step reactive melt infiltration (RMI). The effects of α-SiC addition on the microstructural evolution of the C_f/SiC/PR printed bodies, C_f/SiC/C green bodies, and derived SiC composites were investigated. The results indicate that the added α-SiC particles play an important role in enhancing the flowability of raw powders, reducing the porosity, increasing the reliability of the C_f/SiC/C green bodies, and contributing to improving the microstructure homogeneity and mechanical properties of the SiC composites. The maximum density, flexural strength, and fracture toughness (K_{IC}) of the SiC composites are 2.749±0.006 g·cm^{-3}, 266±5 MPa, and 3.30±0.06 MPa·m$^{1/2}$, respectively. The coefficient of thermal expansion (CTE, α) of the SiC composites is approximately 4.29×10^{-6} K^{-1} from room temperature (RT) to 900 ℃, and the thermal conductivity (κ) is in the range of 80.15–92.48 W·m^{-1}·K^{-1} at RT. The high-temperature strength of the SiC composites increase to 287±18 MPa up to 1200 ℃. This study provides a novel as well as feasible tactic for the preparation of high-quality printable powders as well as lightweight, high-strength, and high-κ SiC composites with complex structures by the SLS and RMI.

Keywords: chopped carbon fiber (C_f); microstructural tailoring; selective laser sintering (SLS); mechanical properties; thermal properties

* Corresponding authors.
E-mail: J. Yin, jieyin@mail.sic.ac.cn;
X. Liu, xjliu@mail.sic.ac.cn;
Z. Huang, zhrhuang@mail.sic.ac.cn

1 Introduction

With the rapid development of space technology, large-scale and lightweight space optical components have become the important components of space-based observation systems, LIDAR systems, and space astronomical telescopes. Different from the traditional optical component materials including glass–ceramic, ultra-low expansion glass, and beryllium (Be), chopped carbon fiber (C_f) reinforced silicon carbide (SiC) composite is gradually becoming the main candidate material for a new generation of space optical components due to its excellent properties such as high specific strength, high reliability, and excellent isotropy [1–3].

Generally, the SiC composites are fabricated by hot pressing (HP), spark plasma sintering (SPS), chemical vapor infiltration (CVI), polymer infiltration pyrolysis (PIP), and reactive melt infiltration (RMI) [4,5]. Among them, the RMI characterized by a low sintering temperature, rapid reaction time, and near-net shaping has been widely applied to the fabrication of the SiC composites. Wang *et al*. [6] fabricated the SiC composites from the carbon cloth by infiltrating phenolic resin (PR), pure carbon slurry, or C/SiC slurry combined with the RMI. Reference [6] indicated that both the flexural strength and fracture toughness (K_{IC}) increased after adding SiC particles from 74.81 to 82.32 MPa and 4.72 to 9.82 MPa·$m^{1/2}$, respectively. Compared with that of the pure carbon preform, the incorporation of SiC particles into the C/SiC preform plays a critical role, acting not only as an inert filler to inhibit the formation of cracks in the pyrolysis process but also as rigid skeleton particles to improve the reliability of the porous bodies [7]. Furthermore, the presence of SiC particles in the initial material recipe can provide seeding sites, favoring the formation of β-SiC during the subsequent RMI process [8].

The desired shape of the SiC composites fabricated by the RMI method depends on the modeling process, including slip casting, dry pressing, and tape casting [9]. However, it is difficult or even impossible to fabricate components with large-scale and complex structures, such as lattice, honeycomb, and topological structures via conventional methods ascribed to the limitation of models. Recently, selective laser sintering (SLS), a promising and moldless three-dimensional (3D)-printing technology, has been applied to near-net shaping SiC composites due to its high efficiency, non-obligatory-additional support structure, high raw material utilization, and flexibility for large-scale and complex-shaped components [10–13]. Especially, the indirect SLS method involving a low-melting-point binder phase has been widely used in the SiC ceramics and their composites [14,15]. Xu *et al*. [16] used the epoxy resin–SiC mixed powders to construct preforms via the SLS, in which epoxy resin acted as a sacrificed binder and was removed during the debinding process. The SiC ceramics were obtained by polycarbosilane (PCS) infiltration and pyrolysis for 9 times and exhibited an excellent high-temperature flexural strength (220 MPa at room temperature (RT) and 203.7 MPa at 1600 ℃) retention. Zhu *et al*. [17] fabricated the SiC composites via the SLS, PR infiltration and pyrolysis, and RMI of the PR-coated C_f composite powders. Reference [18] reported an efficient and novel approach to fabricate SiC composites from the starting materials of C_f and PR mechanical mixing powders. The SLS was used to fabricate C_f/PR printed bodies, which were converted into pure carbon (C_f/C) green bodies in the subsequent debinding process. The dense SiC composites were obtained through an *in-situ* reaction of carbon and silicon in the one-step RMI process. However, the SiC composites exhibited inhomogeneous microstructures due to the poor flowability of printable powders, high open porosity (O), and large pore size distribution of pure C_f/C green body. These could cause the formation of large-scale residual silicon in final products, which could deteriorate the mechanical properties.

In this study, we aim to enhance the flowability of printable powders, improve the reliability of porous green bodies, and regulate the microstructures and comprehensive properties of the SiC composites by compositional tailoring of initially raw composite powders, as well as establishing an efficient, cost-effective, and near-net-shape technique, which is promising to fabricate lightweight, large-scale, and complex-shaped SiC composites. More specifically, α-SiC particles were introduced into the feedstocks for tailoring the microstructures and hence improving the properties. The effects of SiC addition on the flowability of raw powders, microstructural tailoring, and properties of green bodies as well as sintered composites were investigated. Simultaneously, the mechanical property, toughening mechanism, thermal property, and high-temperature flexural strength were also investigated comprehensively.

2 Experimental

2.1 Materials

Commercially available 6H-SiC (H represents hexagonal; 3.2 g·cm^{-3}, D_{50} = 38.9 μm, purity = 99.5 wt%; Shanghai Shangmo Electromechanical Co., Ltd., China) and chopped C_f powders (1.76 g·cm^{-3}, 200 mesh; Shanghai Lishuo Composite Material Technology Co., Ltd., China) were used as the raw materials. The thermoplastic PR (1.22 g·cm^{-3}, D_{50} = 19.5 μm, with a residual carbon yield of 27.9 wt% after binder removal; Shanghai Qi'nan Adhesive Material Factory, China) mixed with the methenamine hardener (10 wt%) was used as the low-melting-point binder in the SLS. The molecular formula of PR is as in Fig. 1.

2.2 Preparation of samples

The C_f, SiC, and PR powders were ball-milled at 66 r·min^{-1} for 1 h using the SiC milling media. The volume fraction (V) of PR was fixed at 25%. Six groups of composite powders with different V of SiC (0%, 15%, 25%, 40%, 50%, and 75%) were prepared, which were labeled as C_f/PR–0 vol% SiC, C_f/PR–15 vol% SiC, C_f/PR–25 vol% SiC, C_f/PR–40 vol% SiC, C_f/PR–50 vol% SiC, and C_f/PR–75 vol% SiC, respectively. The compositions of the C_f/PR–SiC composite powders are shown in Table 1.

The C_f/PR–SiC composite powders with different SiC contents were applied to the SLS of C_f/SiC/PR printed body through the laser printing equipment (Hunan Farsoon High-Technology Co., Ltd., China). The optimized printing parameters are as follows: The laser power, scanning velocity, and hatch distance were 45 W, 7620 mm·s^{-1}, and 80 μm, respectively. The movement direction of the roller was X-axis, the direction of print layer thickness was Z-axis, and Y-axis was perpendicular to the Z–X plane.

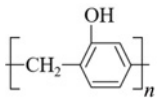

Fig. 1 Molecular structure of PR.

Table 1 Compositions of C_f/PR–SiC composite powders

Composite powders	Material composition (vol%)			Ratio of SiC to inorganic matter (IM), SiC : IM (V_{SiC} : (V_{SiC} + V_{C_f}))
	SiC	C_f	PR	
C_f/PR–0 vol% SiC	0	75	25	0
C_f/PR–15 vol% SiC	15	60	25	0.20
C_f/PR–25 vol% SiC	25	50	25	0.33
C_f/PR–40 vol% SiC	40	35	25	0.53
C_f/PR–50 vol% SiC	50	25	25	0.67
C_f/PR–75 vol% SiC	75	0	25	1

Note: V_{SiC} and V_{C_f} represent the volume fractions of SiC and C_f, respectively.

2.3 Fabrication of SiC composites

The C_f/SiC/PR printed bodies were heat-treated at 1100 ℃ to remove PR binders and obtain porous C_f/SiC/C green bodies under vacuum. After that, Si (2.33 g·cm^{-3}, average size: 1–3 mm) was melted and infiltrated into the porous C_f/SiC/C green body under vacuum at 1550 ℃. Finally, the SiC composites were obtained. The schematic of the fabrication procedures is shown in Fig. 2.

2.4 Characterization

The angle of repose (AOR), apparent density (ρ_0), and tap density (ρ_1) of the composite powders were measured according to the American Society for Testing Material (ASTM) D6393-99, GB/T 16913.3-2008, and GB/T 5162-2006 standards, respectively. The flowability can be characterized according to Carr index and Hausner ratio by Eqs. (1) and (2), respectively:

$$\text{Carr index} = [(\rho_1 - \rho_0)/\rho_1] \times 100\% \quad (1)$$

$$\text{Hausner ratio} = \rho_1/\rho_0 \quad (2)$$

The contents of impurity elements were tested using an inductively coupled plasma mass spectrometer (ICP-MS; iCAP RQ, Thermo Fisher Scientific, USA). The powder size distribution was measured using a laser-diffraction-based particle size analyzer (Malvern Panalytical, UK). The length distribution of C_f was manually measured by the Nano Measurer software, and the number of measurements was ⩾ 100. The morphologies and microstructures of raw powders, C_f/SiC/PR printed bodies, C_f/SiC/C green bodies, and SiC composites with different SiC contents were observed using a scanning electron microscope (SEM; SU8220, Hitachi, Japan) along with an energy dispersive spectrometer for the elemental analysis. The bulk densities (ρ) and O of printed bodies, green bodies, and composites were determined based on the Archimedes principle. The ρ and O can be calculated by Eqs. (3) and (4), respectively:

$$\rho = W_d \rho_w / (W_w - W_s) \quad (3)$$

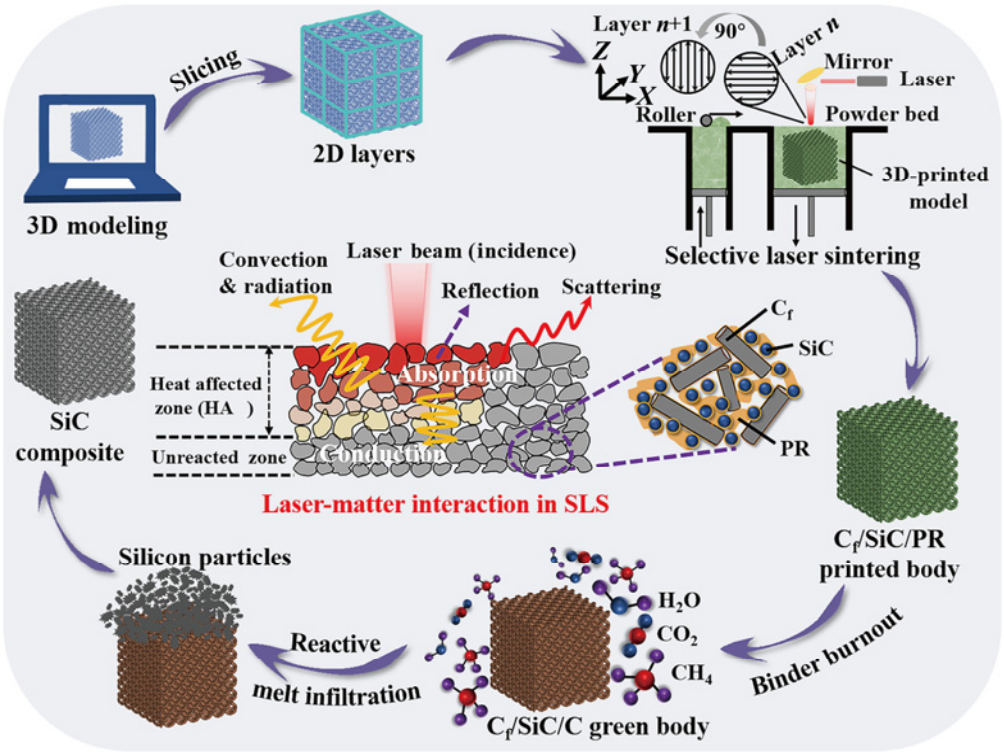

Fig. 2 Schematic diagram of the fabrication of SiC composites.

$$O=[(W_w-W_d)/(W_w-W_s)]\times 100\% \quad (4)$$

where ρ_w, W_w, W_d, and W_s represent the density of deionized water, the wet weight of the sample saturated with water in air, the dry weight of the sample, and the floating weight of the sample in water, respectively.

The volume fraction of residual silicon (V_{Si}) was calculated by Eq. (5):

$$V_{Si}=[(m_1-m_2)\rho_{SiC}]/(2.33m_1) \quad (5)$$

where ρ_{SiC} is the density of the SiC composite, and m_1 and m_2 are the mass of the SiC composites before and after etching in the 1HF:5HNO$_3$ mixture for 72 h, respectively. 2.33 in Eq. (5) represents the density of Si.

The orientation distribution and "Hermans" orientation parameter (f_p) of the C_f in the C_f/SiC/C green body were determined by Eqs. (6) and (7), respectively [19]:

$$<\cos^2\phi>=\int_{-\pi/2}^{\pi/2}\cos^2\phi n(\phi)\mathrm{d}\phi \quad (6)$$

$$f_p=2<\cos^2\phi>-1 \quad (7)$$

where ϕ is the orientation angle, $n(\phi)$ is the fraction of fibers within the angular range (dϕ). The f_p ranges from 0 (random distribution) to 1 (perfect orientation).

A digital caliper with 0.01 mm accuracy was used to measure the dimensional deviation ratio (DDR) of printed bodies and green bodies by Eq. (8):

$$\mathrm{DDR}=[(L-L_0)/L_0]\times 100\% \quad (8)$$

where L_0 is the dimension of the STL model, and L is the measured dimension. Rectangular bars with the dimension of 40 mm (X) × 8 mm (Y) × 6 mm (Z) were used to measure the DDR and subsequent mechanical properties. At least five samples were tested to obtain the average data.

The pore size distributions of the green bodies and the SiC composites after acid corrosion were obtained by a mercury porosimeter (Poremaster60, Micromeritics Instrument Corp., USA). The phase analyses of the SiC composites were performed using an X-ray diffractometer (40 kV, 40 mA; D/max 2550V, Rigaku, Japan) with Cu Kα radiation ranging from 10° to 80°. The oxygen contents of the SiC composites were measured by an oxygen–nitrogen tester (TC600C, Leco Instrument LD, USA).

The flexural strength was measured by a three-point bending test instrument (Instron-1195, Instron, USA) at a crosshead speed of 0.5 mm·min^{-1}, according to the GB/T 6569-2006 and GB/T 10700-2006 standards. The

sample size was 4 mm × 3 mm × 36 mm. The K_{IC} was measured by a single-edge notched beam (SENB) method according to the ASTM C1421-16 standard with a crosshead speed of 0.05 mm·min^{-1}, notch depth of 2.5 mm, and the sample size of 2.5 mm × 5 mm × 36 mm. The high-temperature three-point flexural strengths of the SiC composites were measured at 600, 800, 1000, and 1200 ℃ under an Ar atmosphere using an ultra-high-temperature strength testing machine (AG-X Plus, Shimadzu, Japan). The sample size and crosshead speed were 4 mm × 3 mm × 36 mm and 0.5 mm·min^{-1}, respectively. The heating rate was 33 ℃·min^{-1}. The measurements were performed using a semi-articulating fixture according to the ASTM C1161-13 and ASTM C1211-13 standards.

The coefficient of thermal expansion (CTE, α) values were measured by a thermal dilatometer (DIL402 E, NETZSCH, Germany) from 25 to 900 ℃ at a heating rate of 10 ℃·min^{-1} under an Ar atmosphere. The sample size was 4 mm × 4 mm × 20 mm. The thermal diffusivity (a) was tested from 25 to 900 ℃ under an Ar atmosphere using a laser-flash technique (DLF2800, TA, USA) based on the ASTM E1461 standard. The specific heat capacity (c_p) at RT was measured using a differential scanning calorimeter (DSC; STA 449 F1 Jupiter, NETZSCH, Germany). The sample size was ϕ5.5 mm × 0.5 mm. The c_p at the elevated temperatures were measured based on the ASTM E1269 standard from 25 to 900 ℃ under an Ar atmosphere using a high-temperature c_p analyzer (MHTC96, Setaram, France). The sample size was ϕ4.9 mm × 18 mm. The thermal conductivity (κ) at 25 ℃ can be calculated by Eq. (9) [20]:

$$\kappa = a\rho c_p \tag{9}$$

The density decreases with the increasing temperature, as calculated by Eq. (10) [21]:

$$\rho = \rho_0[1 + 3(\Delta l / l_0) + 3(\Delta l / l_0)^2 + (\Delta l / l_0)^3]^{-1} \tag{10}$$

where ρ, ρ_0, and $\Delta l / l_0$ represent the density at a specific temperature, the density at RT, and the linear α, respectively.

3 Results and discussion

3.1 Powder characteristics

The printable powders with good flowability are critical for successive layer deposition in the SLS. The morphology and granulometry have effects on the flowability. As shown in Figs. 3(a) and 3(b), the C_f is cylindrical with an aspect ratio of 1–30 [22]. The morphology and size distribution of SiC powders are shown in Figs. 3(c) and 3(d), respectively. As shown in Fig. 3(c), the SiC powders are irregular with sharp edges and smooth surfaces. The particles with the relatively small aspect ratios can improve the packing density and flowability [23]. The SiC powders have the

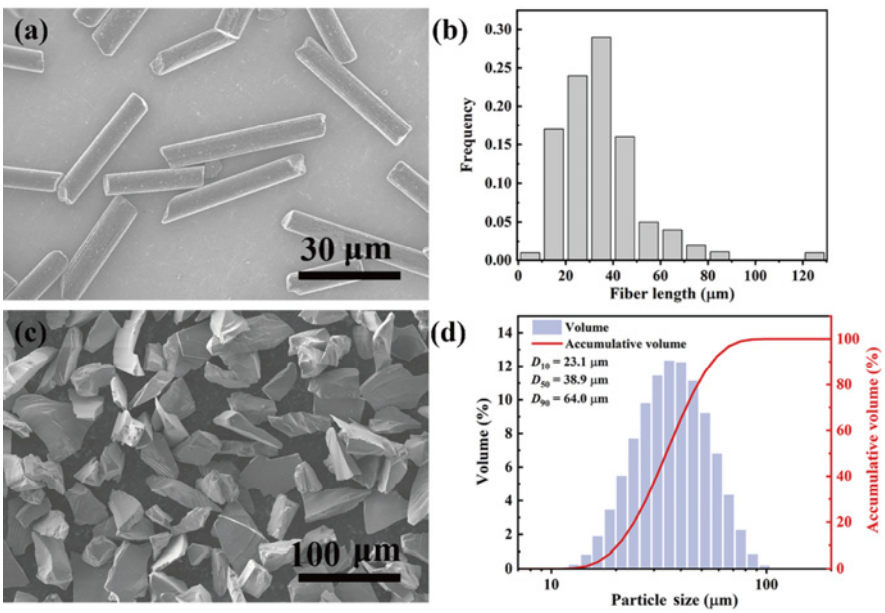

Fig. 3 (a) SEM image of C_f powders; (b) length distribution of C_f powders [22]; (c) SEM image of SiC powders; and (d) PSD of SiC powders.

unimodal and wide size distribution from 11.2 to 98.1 μm, as shown in Fig. 3(d). The particle size distribution (PSD) values of SiC are D_{10} = 23.1 μm, D_{50} = 38.9 μm, and D_{90} = 64.0 μm. The corresponding PSD span (PSD S) is 1.05, which is smaller than 1.5, indicating that the SiC powders exhibit good flowability [24]. The PSD S of PR is 2.61, which is larger than that of SiC particles, leading to more cohesive flowability.

Figure 4 shows the AOR, ρ_0, ρ_1, Carr index, and Hausner ratio results of C_f/PR–SiC composite powders with different SiC contents. As shown in Fig. 4(a), the AOR decreases with the increase of SiC content. And when the SiC:IM $\geqslant$ 0.67, the AOR only slightly changes. Generally, a smaller AOR indicates better flowability. According to Table 2, the SiC raw powders

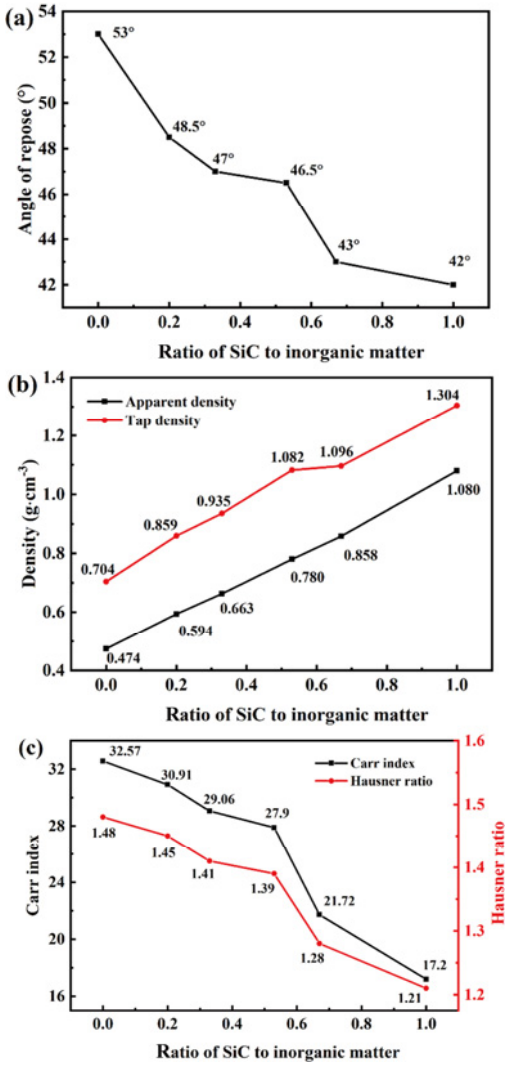

Fig. 4 (a) AOR; (b) ρ_0 and ρ_1; and (c) Carr indexes and Hausner ratios of C_f/PR–SiC composite powders with different SiC contents.

Table 2 Flowability of raw powders

Sample of raw powders	PSD S ($(D_{90}-D_{10})/D_{50}$)	AOR (°)	ρ_0 (g·cm^{-3})	ρ_1 (g·cm^{-3})	Carr index (%)	Hausner ratio
C_f	—	51	0.512	0.769	33.44	1.50
SiC	1.05	37	1.413	1.702	16.95	1.20

exhibit relatively good flowability due to its irregular shapes and large particle size (D_{50} = 38.9 μm) compared with the cylindrical C_f. For the PR, the long molecular chain structure, small particle size (D_{50} = 19.5 μm), large PSD (PSD S = 2.61), and strong inter-particle attractive force (van der Waals force) lead to poor flowability. Therefore, the AOR of SiC:IM = 0 is larger than that of the C_f powders. When the SiC:IM = 0.20, the AOR intensively decreases by 8.5%. As the content of SiC increases further, the AOR of composite powders gradually decreases ascribed to the good flowability of SiC powders.

The ρ_0 and ρ_1, as shown in Fig. 4(b), increase evidently with the increasing SiC content. The ρ_0 is mainly influenced by particle morphology. The higher the sphericity of the particles, the higher the ρ of the powders is. The SiC powders are irregular, so it is easier to achieve dense packing than cylindrical C_f with an aspect ratio of 1–30. Therefore, with the increase of SiC content, the ρ_0 of the composite powders increase significantly and continuously. In the C_f/PR–0 vol% SiC (SiC:IM = 0) composite powders without SiC particles, the ρ_0 is the lowest of 0.474 g·cm^{-3}. In the C_f/PR–75 vol% SiC (SiC:IM = 1) composite powders without C_f, the ρ_0 is the highest of 1.080 g·cm^{-3}. As shown in Fig. 4(b), as the ρ_0 increases, the ρ_1 also increases. The highest ρ_1 is 1.304 g·cm^{-3} when SiC:IM = 1. It can be noted from Fig. 4(b) that the addition of the SiC has a clear effect on the ρ_0 and the ρ_1.

To further characterize the flowability of the C_f/PR–SiC composite powders with different contents of SiC, the Carr index and Hausner ratio are shown in Fig. 4(c). Both the Carr index and Hausner ratio decrease with the rise of the SiC content. The smaller the Carr index and Hausner ratio, the better the flowability is. The results indicate that the added SiC particles can act as the "lubricant" to improve the flowability of the composite powders.

3.2 Microstructural evolution and properties of C_f/SiC/C green bodies

The microstructures of C_f/SiC/PR printed bodies with

different SiC contents are shown in Fig. 5. The C_f/SiC/PR printed bodies show the porous structures with connected pores, and the melted PR is coated on the surfaces of the C_f and SiC particles, forming "SLS necks" to bond powders together, as shown in Figs. 5(e) and 5(f). With the addition of SiC powders, since the surface of SiC enriches numerous reactive –Si–OH oxygen-containing functional groups with higher surface free energy than the inert surface of C_f [25], the competing effect leads to more and more PR coated onto the SiC surface, and then the sharp edges of SiC particles become blur and rounded. Therefore, the surface of SiC becomes further rougher due to coating with PR. Figure 5(b) shows that SiC particles are uniformly dispersed and connected to C_f through the viscous flow of PR. When the SiC:IM increases to 0.67, the PR-coated SiC particles are bonded together forming aggregates, as shown in the red circles in Fig. 5(e). Moreover, based on the microstructural control, since SiC particles fill into the pores of the C_f skeleton, therefore, the porosity decreases gradually with the increase of SiC content, as shown in Fig. 5.

Figure 6 shows the representative microstructure and orientation distribution of the C_f/SiC/C (SiC:IM = 0.2) green body. After pyrolysis, PR was converted into pyrolytic carbon (PyC) and pores. Simultaneously, the C_f and SiC surfaces become smoother than those of the printed bodies due to the chemical bond reorganization [17], as shown in Fig. 6(a). The PyC bonds the C_f and SiC particles together, as shown in the inset of Fig. 6(a). Combined with the aforementioned analysis, the PR-coated C_f and SiC printed bodies are converted into PyC-coated C_f and SiC porous green bodies after pyrolysis; therefore, there is an obvious color change from green to black after pyrolysis for the sample of SiC:IM = 1 without C_f addition. Figure 6(b) shows the orientation distribution of C_f along the *X*-axis, which shows that the fibers are evenly distributed between all angles. The f_p calculated by Eqs. (6) and (7) is 0.12, which further confirms that the fibers are distributed isotopically and randomly in this study.

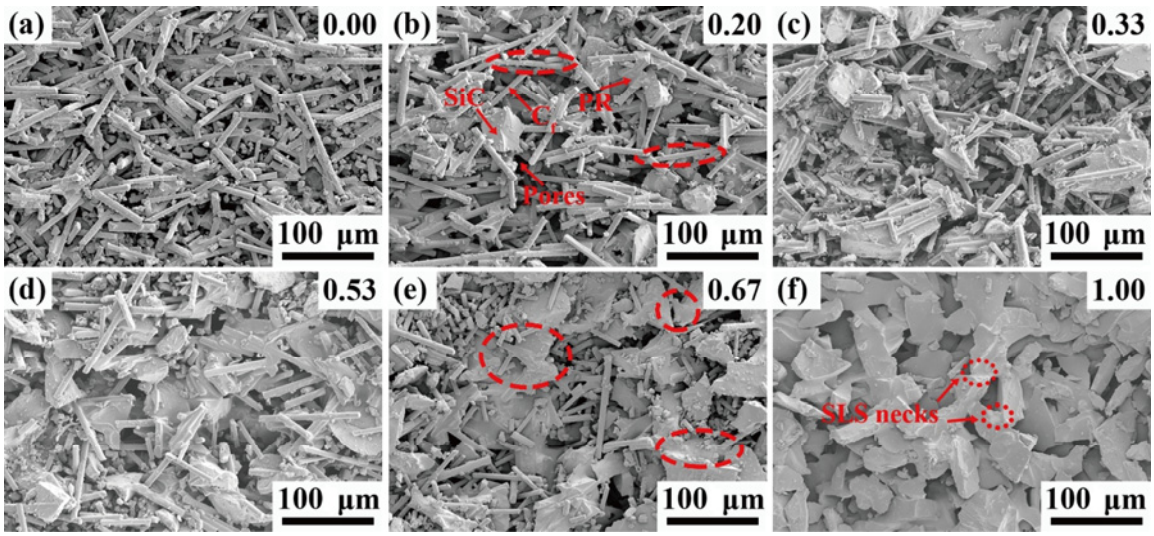

Fig. 5 Morphologies of C_f/SiC/PR printed bodies with different SiC contents: (a) SiC:IM = 0; (b) SiC:IM = 0.20; (c) SiC:IM = 0.33; (d) SiC:IM = 0.53; (e) SiC:IM = 0.67; and (f) SiC:IM = 1.

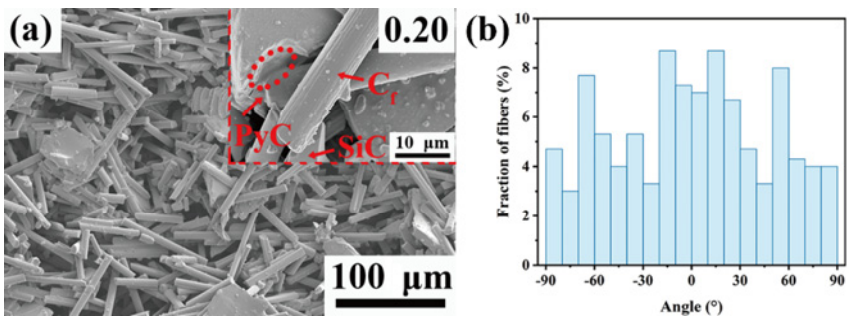

Fig. 6 (a) Representative morphology of C_f/SiC/C green body (SiC:IM = 0.20); (b) C_f orientation distribution corresponding to (a).

The SiC content has an effect on the physical properties of C_f/SiC/C green bodies, including dimensional accuracy, microstructure, and mechanical property. Figure 7 shows the DDR results of the C_f/SiC/C green bodies in length (*X*), width (*Y*), and height (*Z*) directions. When the SiC:IM = 0, the DDR shows a positive deviation in both *X* and *Y* directions. The reason for the positive deviation is that the residual heat of the laser bonds the neighboring excess powders together, resulting in excessive densification during the SLS process. However, when the SiC:IM = 0.2, the dimension deviations in *X* and *Y* directions gradually convert into negative deviations and continue to decrease with the increasing SiC content. With the increase of SiC content, on the one hand, the multiple

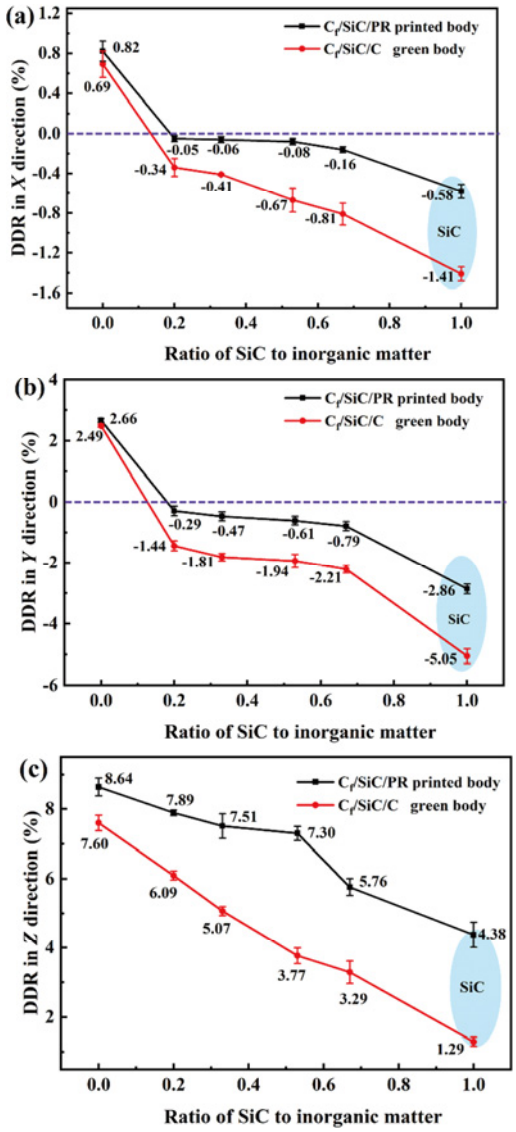

Fig. 7 (a) DDRs in *X* direction; (b) DDRs in *Y* direction; and (c) DDRs in *Z* direction.

reflections of the powders on the laser are weakened, resulting in the decrease of the laser absorption of the composite powders. Under the same laser energy density, the depth and width of the molten pool decrease, and the diffusion of the heat-affected zone decreases [26]. On the other hand, the "connective" effects of C_f gradually weaken. Therefore, the DDR decreases. Thus, the SiC:IM = 1 sample without C_f powders exhibits the highest DDRs of −0.58% and −2.86% in the *X* and *Y* directions, respectively. Because the *X* direction is the paving powder direction, the powders have a tendency to self-compact along with the *X* direction; therefore, the DDRs in the *X* direction exhibit lower than those in the *Y* direction. Additionally, the DDRs in the *Z* direction are relatively higher than those in the *X* and *Y* directions. This is mainly due to the laser penetration effect induced by the temperature variation of the thermal conduction gradient along the *Z* direction between the printing layer and as-printed layer. Moreover, heat penetration along the *Z* direction would result in the excess binding of adjacent as well as sub-adjacent unprinted layers, which is different from *X* and *Y* directions. It should also be noted that the printed green bodies experienced further shrinkage after subsequent pyrolysis process. According to Ref. [27], the RMI has been known as a near-net-shape forming method with less line shrinkage (≤ 1%).

The pore diameters of porous C_f/SiC/C green bodies are important for the subsequent RMI. Figure 8 shows the pore size distributions of the C_f/SiC/C green bodies varying with the SiC content. All the C_f/SiC/C green bodies show the broad and unimodal pore size distributions from 10 to 35 μm, which indicate that the green bodies possess homogeneous pore channels. The median pore diameter (MPD) varies from 18.77 to 28.72 μm, while the average pore diameter (APD) varies from 468.4 nm to 12.2 μm. With the increasing SiC content, the pore size distribution narrows down initially before widening up, and the MPD first decreases, and then increases. When the SiC:IM increases to 0.33, the MPD achieves a minimum of 18.77 μm, and the corresponding APD is 504.3 nm. In this study, the pores are produced by the stacking of C_f and SiC particles as well as debinding of PR. Under the fixed PR content, it can be considered that the pore size distributions of the porous C_f/SiC/C green bodies are mainly affected by the particle stacking pore. When the SiC:IM ≤ 0.33, the C_f acts as a skeleton phase

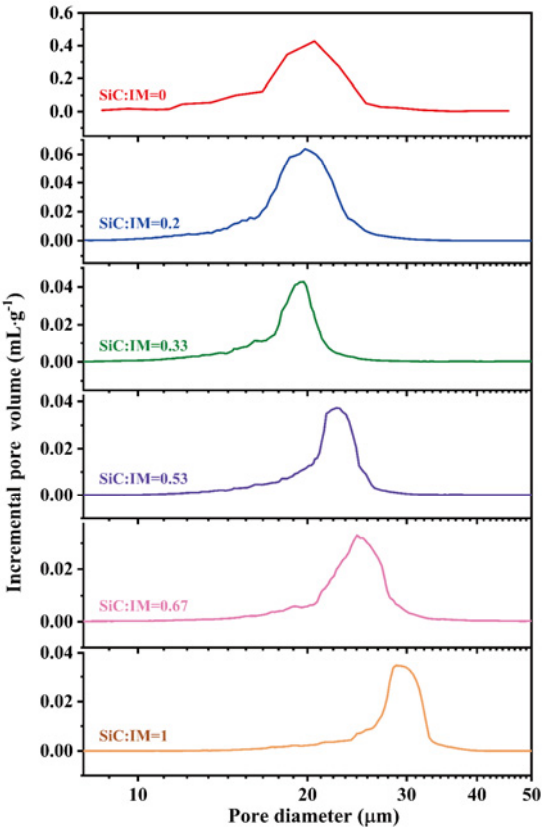

Fig. 8 Pore size distributions of C_f/SiC/C green bodies.

that can encapsulate SiC particles and fill the voids between the particles, resulting in the decrease of MPD. When the SiC:IM further increases to 1, the "connective" effects of C_f gradually weaken due to the decrease of C_f content, resulting in the gradual increase of MPD.

Combined with Ref. [18], the thermodynamical parameters including the capillary force and infiltration depth in the RMI process can be calculated. The penetration depth increases with the increasing pore size, while the corresponding capillary driving force decreases. The maximum capillary force is 6.09×10^6 N, and the corresponding infiltration depth in one second reaches a minimum of 13.13 mm for the SiC:IM = 1 green body, indicating that the RMI is a very rapid process.

Figure 9 shows the porosity, ρ, and flexural strengths of C_f/SiC/C green bodies with different SiC contents. As shown in Fig. 9(a), the O of the C_f/SiC/C green bodies decreases with the increase of SiC content, while the ρ shows the opposite trend. Notably, the ρ of C_f/SiC/C green body is very close to the ρ_0, but lower than the ρ_1 of corresponding C_f/PR–SiC composite powders. The static and dynamical wall effects cause a large number of pores in the powder layer during the powder-spreading process [28]. As a powder-spreading additive manufacturing technique, the O of printed C_f/SiC/C green body is related to the flowability of the C_f/PR–SiC composite powders. With the increase of SiC content, the flowability of composite powders increases gradually, and thus the O of C_f/SiC/C green body decreases. Simultaneously, since the C_f is cylindrical with an aspect ratio of 1–30, it is difficult to achieve dense packing, so the SiC:IM = 0 sample without any SiC particles shows the highest O and lowest ρ of 74.89%±0.1% and 0.449±0.003 g·cm^{-3} [18], respectively. The added irregular SiC particles can fill in the pores forming from the C_f skeletons; therefore, the porosity of C_f/SiC/C green bodies is significantly reduced from 74.89% to 67.29%. The abundant porosity provides the infiltrative channels for the subsequent RMI.

Figure 9(b) shows the flexural strengths of the C_f/SiC/C green bodies. As shown in Fig. 9(b), the flexural strengths of green bodies first increase by 22.21% and 7.65% when the SiC:IM increases to 0.20 and 0.33, respectively. When the SiC:IM increases to 0.20, the C_f can dissipate the energy of crack propagation and deflect the crack [29];

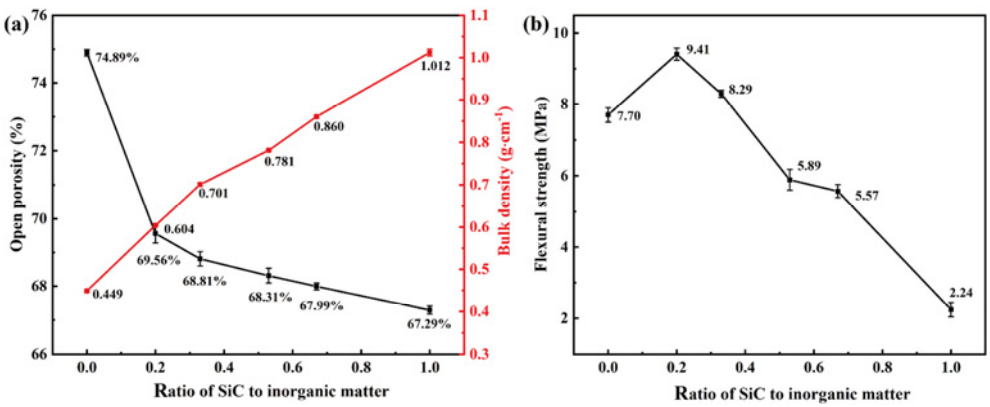

Fig. 9 (a) O and ρ and (b) flexural strengths of C_f/SiC/C green bodies with different SiC contents.

meanwhile, the C_f acts as a skeleton phase that can encapsulate the SiC particles and fill the voids between the particles, that is, the C_f and SiC particles synergistically improve the flexural strength. Additionally, according to the Ryskewitch–Duckworth relationship ($\sigma \propto e^{-bP}$) [30], the strengths of porous materials have the negative exponential relationships with porosity, and the decrease in the O of C_f/SiC/C green bodies also contributes to the increase in the strength (SiC:IM $\leqslant$ 0.2). When the SiC:IM further increases from 0.53 to 1, although the O of C_f/SiC/C green bodies decreases continuously, the strength of C_f/SiC/C green bodies is lower than that of the sample of SiC:IM = 0 without SiC particles due to the loose microstructure, large pore size, and weak "connective" effect of C_f. The maximum flexural strength of 9.41± 0.17 MPa is finally achieved for the SiC:IM = 0.2 green bodies. These flexural strength results coincide with the obtained microstructures from the SEM analysis (Fig. 5) and the pore diameter distributions of C_f/SiC/C green bodies (Fig. 8).

3. 3 Microstructural evolution and phase compositions of SiC composites

The microstructures and element distributions of the SiC composites are shown in Fig. 10. All the SiC composites consist of SiC (dark-gray), residual silicon (light-gray), and carbon (black). The SiC:IM = 0 sample shows a relatively heterogeneous element distribution with a large amount of "Si lake", as shown in Fig. 10(a). As mentioned in Section 3.2, the corresponding green body (SiC:IM = 0) has a high porosity (74.89%±0.1%) and large pore diameter (MPD = 21.04 μm), which subsequently lead to a heterogeneous microstructure in the SiC:IM = 0 sample. With the increase of SiC content in the starting materials, the microstructure homogeneity of the SiC composites is improved, as shown in Figs. 10(b)–10(h). Figures 10(c) and 10(d) show the high-magnification SEM micrograph and energy dispersive spectroscopy (EDS) mapping of the SiC:IM = 0.2 sample, respectively; in addition to SiC, residual Si, and C, a small amount of bright-white region is also observed, which is analyzed by the EDS as Al–Fe alloys originating from impurities in the raw materials, as shown in Table 3.

During the RMI process, the liquid silicon infiltrates into the porous C_f/SiC/C green bodies driven by capillary forces and reacts with the carbon *in-situ* to form SiC based on Reaction (11).

$$\alpha\text{-SiC} + \text{Si} + \text{C} \rightarrow \text{SiC} \tag{11}$$

The initial addition of SiC particles can act as grain seeds to induce the formation of β-SiC [8]. Moreover, the reaction-formed SiC shows a fine PSD of 0.5–10 μm in the SiC:IM = 0 sample without α-SiC addition, as shown in Fig. 10(a). Thus, with the increase of SiC content, the amount of large-sized α-SiC particles (D_{50} = 38.9 μm) increases, since the grain size of SiC obtained by the RMI was merely 0.5–10 μm. Additionally, it should be noted that with the increasing SiC content, the amount of residual silicon first decreases (SiC:IM $\leqslant$ 0.33), and then increases (SiC:IM > 0.33), which coincides with the pore diameter distributions of C_f/SiC/C green bodies.

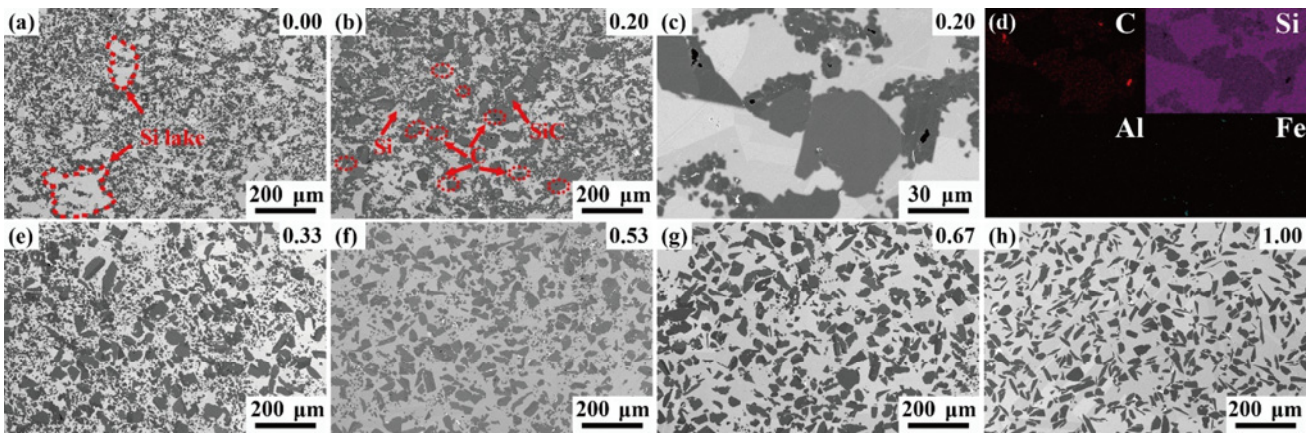

Fig. 10 Polished surface morphologies of SiC composites (back-scattered electron SEM): (a) SiC:IM = 0; (b) SiC:IM = 0.20; (e) SiC:IM = 0.33; (f) SiC:IM = 0.53; (g) SiC:IM = 0.67; and (h) SiC:IM = 1. (c) High-magnification SEM micrograph of SiC:IM = 0.20. (d) EDS mappings of SiC:IM = 0.20.

Table 3 Properties of raw powders

Impurity	C_f	SiC	PR	Si
Fe (wt%)	0.15 [18]	0.19	0.01 [18]	0.44
Al (wt%)	< 0.001 [18]	0.019	< 0.001 [18]	0.13
Si (wt%)	< 0.005	—	< 0.005	—

The X-ray diffraction (XRD) patterns show the phase compositions of the obtained SiC composites, as shown in Fig. 11. The SiC raw powders have a hexagonal cell (α-SiC, 6H) with a lattice parameter of 3.079 Å × 3.079 Å × 15.109 Å. The SiC composite fabricated by the SiC:IM = 0 sample without initial SiC addition is mainly composed of β-SiC (3C) and residual Si. The characteristic diffraction peaks of α-SiC at about 2θ = 34.13° and 38.16° are detected in the SiC composites after adding SiC particles. Furthermore, the residual carbon and Al–Fe alloy impurities observed in the SEM images are not detected in the XRD patterns, indicating that their contents are less than 5 wt%.

To quantitatively analyze the phase volume percentage of the SiC composite, we used the acid mixture (1HF:5HNO_3) to etch residual silicon for 72 h at RT, as shown in Reaction (12).

$$3Si + 4HNO_3 + 12HF = 3SiF_4 + 4NO + 8H_2O \quad (12)$$

The SiC has the high-temperature-stable α-SiC (2H, 4H, and 6H) phase and low-temperature-stable β-SiC (3C, where C represents cubic) phase polymorphy, and a remarkable phase transition from β-SiC to α-SiC occurs when the temperature exceeds 2000 ℃ [31]. Based on Ref. [18], the theoretical phase volume percentage can be obtained by combining the volume expansion of the infiltration process without considering the phase transition and residual pores. The quantitative phase volume percentage of the SiC composites based on the theoretical calculation and experimental measurement are listed in Table 4.

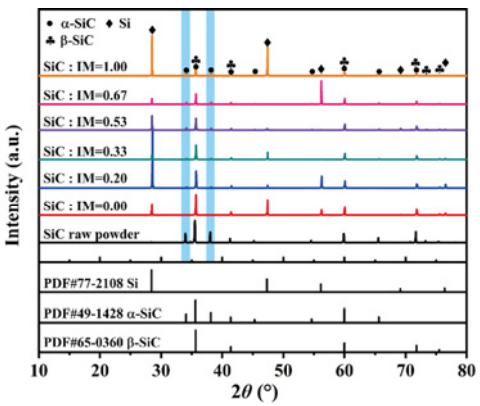

Fig. 11 XRD patterns of SiC composites.

Table 4 Phase compositions of SiC composites

Sample	Theoretical parameter		Experimental parameter
	Total SiC (vol%)	Residual Si* (vol%)	Residual Si (vol%)
SiC:IM = 0	47	53	56.72±0.78
SiC:IM = 0.20	49.84[a]	50.03	50.31±0.26
SiC:IM = 0.33	50.15	49.85	52.40±0.39
SiC:IM = 0.53	45.06	54.94	60.48±0.76
SiC:IM = 0.67	43.02	56.98	61.68±0.81
SiC:IM = 1	35.08	64.92	—

Note: [a]The residual carbon content is 0.13 vol% measured by the image method in the representative SiC composite (SiC:IM = 0.20).

As shown in Table 4, the content of theoretical residual Si first decreases (SiC:IM ⩽ 0.33), and then increases (SiC:IM ⩾ 0.53) with the increasing addition amounts of SiC powders, which is consistent with the changing trend of pore diameters of C_f/SiC/C porous green bodies. When the SiC:IM increases to 0.33, the experimentally measured residual Si content is very close to the theoretically calculated values, and the deviation is ⩽ ±3%. However, when the SiC:IM further increases from 0.53 to 1.0, the measured Si content is much higher than the calculated ones. The reason can be explained as follows: During the RMI, the silicon reacts with carbon to obtain SiC, resulting in volume expansion. The excess pores are filled with liquid silicon. The HF–HNO_3 mixture can etch free silicon and only retain SiC and residual carbon. As the pore size of the C_f/SiC/C porous green bodies increases, the size of free silicon also increases. For SiC:IM ⩾ 0.53 samples, it is difficult to maintain the bulk form for the porous SiC skeleton after corrosion due to the large pore size distribution of the corresponding C_f/SiC/C green bodies, resulting in that some SiC particles are precipitated in the etching solution, so the measured residual Si content is much higher than the theoretical parameters. Additionally, for the SiC:IM = 1 sample, the residual silicon content could not be determined by etching due to the large pore size of the corresponding green body. Meanwhile, the residual carbon contents in representative SiC composites (SiC:IM = 0.20) before and after the RMI have been tested by the image method, which are 25.42 and 0.13 vol%, respectively, as shown in Table 4. The amount of C_f decreases after the RMI due to corrosion of C_f by liquid silicon, resulting in the not quite high K_{IC}. Based on the differed applications, superior K_{IC} is not critically required, such as for space optical and nuclear usages. However, it is difficult to deposit SiC

or BN coating on the surface of the chopped C_f by the CVI technique like the continuous C_f woven into blocks. Therefore, the chopped C_f is corroded during the RMI process (with the purpose of reducing the fabrication cost as well). Further systematic investigation is currently conducted by adopting CVI technique to fabricate SiC, BN, or PyC-coated C_f to prevent corrosion of C_f during the RMI.

Additionally, we analyzed the mean grain size (MGS) of β-SiC after acid corrosion, the MGS of β-SiC in the SiC:IM = 0.20 sample decreases compared with that of the SiC:IM = 0 sample, and the MGSs of β-SiC are 4.0 and 5.54 μm, which indicate that the addition of α-SiC can inhibit the growth of β-SiC grain. According to Ref. [32], the Zener pinning effect at grain boundaries could exert a pinning pressure to counteract the driving force of grain boundary movement, and thus inhibit grain boundary migration, indicating that the added α-SiC suppresses the grain boundary migration and the growth of β-SiC by pinning the grain boundaries.

3.4 Mechanical and thermal properties of SiC composites

Figure 12 shows the RT mechanical properties (i.e., O, ρ, flexural strength, and K_{IC}) parallel to the printing layer of the SiC composites. As shown in Fig. 12(a), all the SiC composites show the similar O within 1%, indicating complete densification. Since the density of composites conforms to the mixing rule, the ρ of the SiC composites initially increases, and then decreases with the increasing SiC, coinciding with the experimentally measured residual Si content, as shown in Table 4, among which the SiC:IM = 0.20 sample has the maximum value of 2.749±0.006 g·cm^{-3}. As shown in Fig. 12(b), the flexural strength and K_{IC} of the SiC:IM = 0 sample are 266±5 MPa and 2.87±0.07 MPa·m$^{1/2}$ [18], respectively. The flexural strength gradually decreases with the increase of SiC content. The flexural strength of the SiC composites fabricated by the RMI is related to the grain sizes of SiC and residual Si content. According to the Hall–Petch relationship ($\sigma \propto d^{-1/2}$) [33], when the SiC:IM increases to 0.33, although the residual Si content decreases, the flexural strength decreases because the particle size of the initially added SiC (D_{50} = 38.9 μm) is much larger than that of reaction-formed SiC (0.5–10 μm). With further increase of SiC:IM to 1, the flexural strength decreases further under the effect of the gradual increase of the residual Si content and the gradual increase of the SiC grain size. The K_{IC} of the SiC composites first increases with the SiC content in the starting materials, and then decreases. The SiC:IM = 0.20 sample has the highest K_{IC} of 3.30±0.06 MPa·m$^{1/2}$ and high flexural strength of 250±11 MPa. Compared with that of the SiC:IM = 0 sample (without the introduction of SiC raw powders), its K_{IC} increases by 15%. By analyzing the pores of the SiC composites after acid corrosion, the grain size of the residual Si in SiC:IM = 0.20 specimen is found to decrease significantly in comparison with that of SiC:IM = 0 counterpart, with the corresponding APDs to be 52.93 nm and 4.43 μm, respectively, which are consistent with the aforementioned SEM results. The addition of SiC raw powders can effectively avoid the formation of large-sized "Si lakes" and further improve the microstructural homogeneity, thus leading to enhanced K_{IC}. Furthermore, we tested the mechanical properties perpendicular to the printing layer. The ρ, flexural strength, and K_{IC} of the SiC:IM = 0.20 sample are 2.774±0.003 g·cm^{-3}, 241±9 MPa, and 3.49±0.08 MPa·m$^{1/2}$, respectively. Although the SLS is a layer-by-layer stacking method along the Z direction, there is

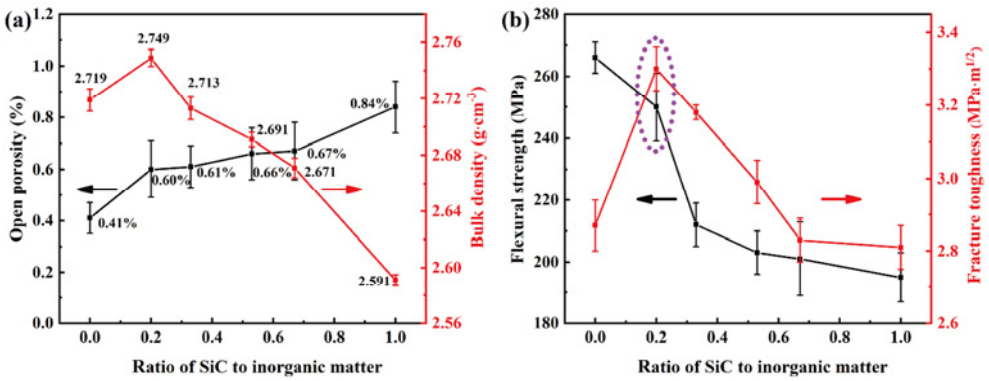

Fig. 12 RT mechanical properties of SiC composites: (a) O and ρ and (b) flexural strength and K_{IC}.

a slight difference in mechanical properties in different directions. Compared with other SiC-based composites fabricated by additive manufacturing [17,18,34,35], this study shows a higher flexural strength and K_{IC}.

The fracture-surface morphologies of the SiC composite are used to elucidate the fracture mechanism of the SiC composites. Figure 13 shows the typical fractured surfaces of the SiC:IM = 0.20 composite after the bending tests. As shown in the red circles in Fig. 13(a), residual C_f embedded within the β-SiC grains can be observed. The thermodynamic calculation by HSC Chemistry version 6.0 (Outokumpu Research Oy, Finland) shows that the Gibbs free energy change (ΔG) of the silicon–carbon reaction, as shown in Reaction (11), is about −12.641 kcal at 1550 ℃, indicating that the reaction between carbon and silicon is spontaneous. It is worth noting that the activity of the carbon source also affects the formation of β-SiC. During the RMI, the liquid Si preferentially reacts with the PyC, and then reacts with the surficial layer of C_f to form the β-SiC layer, which can act as a barrier against the diffusion of liquid silicon and further siliconization of C_f. For this reason, the residual C_f is embedded within the β-SiC grains, as shown in Fig. 13(b). Simultaneously, the β-SiC layer of the C_f surface and the α-SiC layer of the matrix form the strong interface bonding, and the crack perpendicular to the fiber will penetrate into the fiber, releasing the elastic strain energy [29]; therefore, obvious fiber breakages are detected. Moreover, the SiC matrix shows typical transgranular fractures.

The κ and α are the key thermal properties of the SiC composites as important components in space optical systems. Figure 14 shows the thermal properties

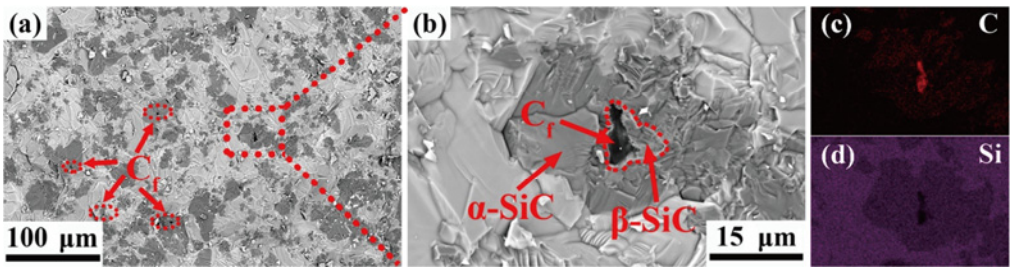

Fig. 13 Fractured morphologies of SiC composite with SiC:IM = 0.20: (a) back-scattered electron SEM; (b) high-magnification SEM micrograph; and (c, d) EDS mappings.

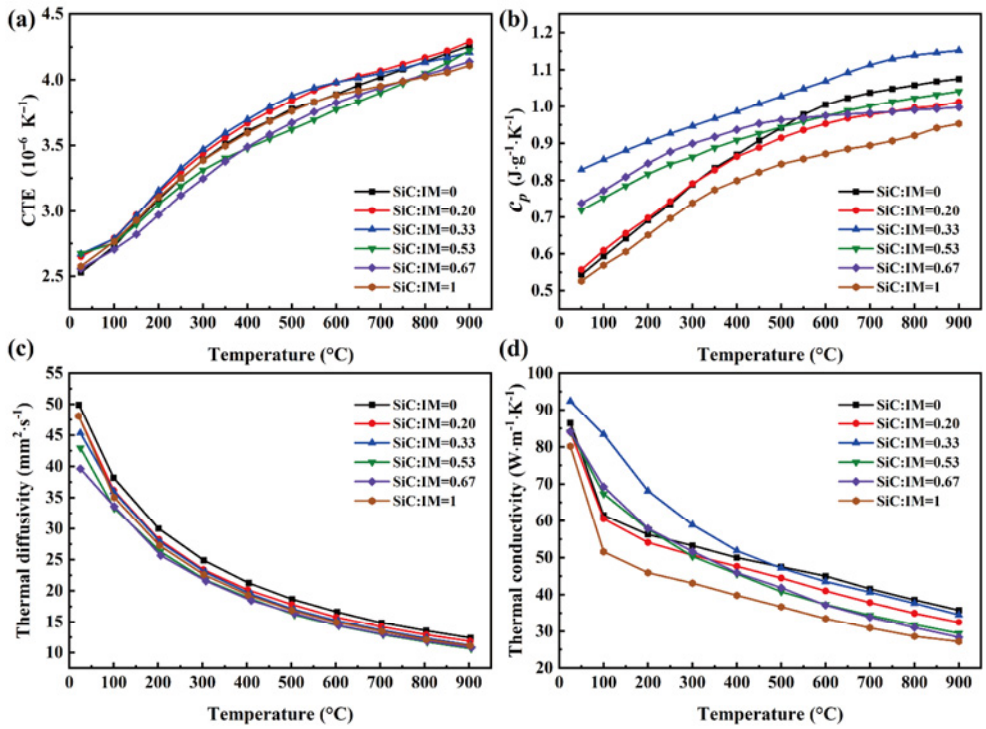

Fig. 14 Thermal properties of SiC composites: (a) α; (b) c_p; (c) a; and (d) κ.

of the SiC composites parallel to the printing layer. As shown in Fig. 14(a), the α value increases over the entire temperature range, which is lower than 4.3×10^{-6} K^{-1} (average linear α of the SiC composites, RT–900 ℃). According to Refs. [36,37], the α of Si and SiC are 2.6×10^{-6} and 3.3×10^{-6} K^{-1} at RT, respectively. Thus, the α of the SiC composites increase slightly with the increasing SiC fraction. Although the SiC:IM = 0.20 sample has relatively the highest α of 4.29×10^{-6} K^{-1} due to its highest total SiC fraction among all samples (Table 4), its α is still in low level. Furthermore, for the sample with the recipe of SiC:IM = 0.20, its α measured perpendicular to the printing layer is 4.39×10^{-6} K^{-1}, which is also comparable with that measured parallel to the printing layer direction.

The c_p, a, and κ of the SiC composites were measured from RT to 900 ℃, as shown in Figs. 14(b)–14(d). The c_p increases with temperature for the SiC composites, which coincides with the Debye theory [20]. While the a shows the inverse temperature dependence, indicating that the phonon conduction behavior dominates in the SiC composites. And the a of SiC:IM = 0 sample is in the range of 12.39–48.97 $mm^2 \cdot s^{-1}$ from RT to 900 ℃, the highest among all the SiC composites reported in this study. The RT κ of the SiC composites in this study is in the range of 80.15–92.48 $W \cdot m^{-1} \cdot K^{-1}$, and the SiC:IM = 0.33 sample has the highest κ of 92.48 $W \cdot m^{-1} \cdot K^{-1}$. As the temperature increases to 900 ℃, the κ monotonously decreases to 27.21–35.81 $W \cdot m^{-1} \cdot K^{-1}$. As the temperature increases, the vibration frequency of the phonon increases, and the scattering effect increases, so the free path decreases, and the κ decreases. The RT κ of the SiC composites is relatively lower than those of the reported values of pressureless sintered SiC (160–180 $W \cdot m^{-1} \cdot K^{-1}$) [38] and hot-pressed SiC (120 $W \cdot m^{-1} \cdot K^{-1}$) ceramics [39], but better than those of the wood-derived Si/SiC composite (70 $W \cdot m^{-1} \cdot K^{-1}$) from wood [20] and the SiC composite (74–84 $W \cdot m^{-1} \cdot K^{-1}$) fabricated by the SLS–PIP–RMI hybrid route due to the homogeneous microstructure [34]. There are three main reasons for the low κ of the SiC composites in this study. The first reason is the presence of PyC (about 3 $W \cdot m^{-1} \cdot K^{-1}$, RT) as a poor thermal conductor [40]. And then, according to the aforementioned phase composition and microstructure analysis, the SiC composites are mainly composed of three-phase SiC, residual silicon, and residual carbon. The phase interface can cause the phonon scattering and low κ. Additionally, the defects including pores and impurities (Al–Fe alloys) induce phonon scattering, resulting in the decrease of mean free path and κ.

The high-temperature flexural strengths of the SiC composite (SiC:IM = 0.20) were measured at 600, 800,

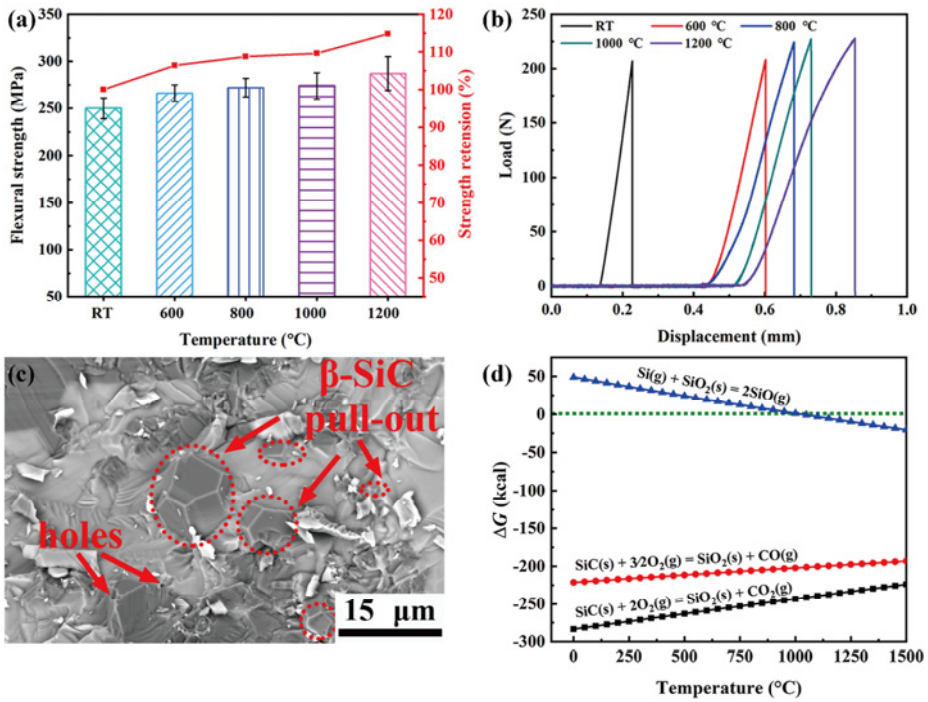

Fig. 15 (a) Flexural strengths of SiC composite (SiC:IM = 0.20) at RT, 600, 800, 1000, and 1200 ℃; (b) load–displacement curves of SiC composite (SiC:IM = 0.20) in (a); (c) fracture surfaces at 1200 ℃; and (d) ΔG of Reactions (13)–(15).

1000, and 1200 ℃ under an Ar atmosphere (Fig. 15). As shown in Fig. 15(a), the flexural strengths of the SiC composites at RT, 600, 800, 1000, and 1200 ℃ are 250±11, 266±9, 272±10, 274±11, and 287±18 MPa, respectively. As the temperature increases, the flexural strength increases and reaches the maximum at 1200 ℃. The strength retention is 114.8% at 1200 ℃. The increase in strength at elevated temperatures might be due to the crack healing effect [41]. Compared with the other SiC-based composites fabricated by laser additive manufacturing [16], the present material shows a higher high-temperature strength and retention due to the homogeneous microstructure and low porosity (0.6% vs. 19.1%).

Figure 15(b) shows the load–displacement curves of the flexural strength tests at different temperatures. It can be seen that the curves for different conditions of RT, 600, 800, and 1000 ℃ samples are almost linear up to the maximum load, and then followed by sharp load decrease, exhibiting brittle fracture due to the strong interface bonding between the α-SiC and β-SiC layers of the C_f surface. However, the load–displacement curve for 1200 ℃ sample exhibits significant non-linear tendency up to the maximum load, indicating the creep behavior of Si. Moreover, the displacement to the failure of the RT sample is less than 0.3 mm, while the 1200 ℃ sample shows the increased displacement to the failure up to 0.85 mm ascribed to the plastic deformation of residual Si.

The fractured surface of the 1200 ℃ sample is shown in Fig. 15(c). The β-SiC grains and holes can be observed clearly due to the pullout of SiC. Therefore, the SiC matrix is the intergranular failure at 1200 ℃. The transition of fracture mode might be related to the weakening of the bonding strength between the Si and SiC interface at elevated temperatures [41]. Meanwhile, the oxygen contents in the samples after high-temperature strength testing first slightly increase from 2.64 to 2.73 wt% from RT to 800 ℃, and then decrease to 1.92 wt% at 1200 ℃. Notably, when the temperature is below 1200 ℃, the SiC will undergo passive oxidation to form solid SiO_2 [42]. The relevant reactions involved in the high-temperature bending tests are shown in Reactions (13)–(15).

$$SiC(s) + 2O_2(g) = SiO_2(s) + CO_2(g) \quad (13)$$

$$SiC(s) + 3/2O_2(g) = SiO_2(s) + CO(g) \quad (14)$$

$$Si(g) + SiO_2(s) = 2SiO(g) \quad (15)$$

To further investigate the oxidation mechanism in this study, the ΔG of the reactions at various temperatures (0–1500 ℃) was calculated by the HSC Chemistry software, as shown in Fig. 15(d). Generally, a negative ΔG indicates that the reaction is spontaneous. As shown in Fig. 15(d), the ΔG of Reactions (13) and (14) are negative within 0–1500 ℃, while the ΔG of Reaction (15) is positive at 0–1000 ℃. As the temperature exceeds 1000 ℃, ΔG of Reaction (15) changes to negative. Therefore, the increase in oxygen content is mainly due to the passive oxidation of SiC to form SiO_2; and when the temperature exceeds 1000 ℃, Reaction (15) is spontaneous, and the formation of SiO vapor leads to a decrease in oxygen content. Additionally, the study by Ness and Page [43] showed that impurity elements including K, Ca, Al, and Fe tend to form amorphous phases at the Si/SiC interface. At high temperatures, the softening of the amorphous phase leads to the weakening of the interface bond strength. At this time, the crack can propagate along the Si/SiC interface, forming the intergranular failure. The formation of SiO_2 as well as the mismatch of α [44] between Si- and SiC-induced crack healing effects and the change of the fracture mode is beneficial to the improvement of high- temperature strength.

As shown in Table 5, compared with the SiC composites fabricated by different additive manufacturing methods, enhanced mechanical and thermal properties

Table 5 Comparison of mechanical and thermal properties by different additive manufacturing techniques

Method	Composition	Density ($g \cdot cm^{-3}$)	Flexural strength (MPa)	K_{IC} ($MPa \cdot m^{1/2}$)	κ ($W \cdot m^{-1} \cdot K^{-1}$)	Ref.
SLS+RMI	SiC composites	2.749	266	3.30	92.48	This work
SLS+PIP+RMI	C_f/SiC	2.83	249	3.48	—	[17]
SLS+PIP+RMI	C_f/SiC	2.89	237	3.56	84	[34]
SLA+RMI	C_f/SiC	2.75	262	1.80	—	[35]
SLA+RMI	C_f/SiC	2.69	250	3.46	—	[46]
DIW+RMI	SiC	2.94	224	—	112	[45]
DIW+CVI+RMI	C_f/SiC	—	274	5.82	—	[47]

Note: SLA is the abbreviation of stereolithography, and DIW is the abbreviation of direct ink writing.

in combination with the relatively lower density are measured for our SiC composites compared with Ref. [34], such as SiC composites fabricated by using SLS+PIP+RMI method or SiC ceramics fabricated by direct ink writing (DIW)+RMI technique [45]. The reason is mainly due to the homogeneous microstructure and lower sintered porosity (0.6% vs. 2.1%).

The STL models and sintered components of turbine blades and mirrors with complex structures are shown in Fig. 16. These results indicate the flexibility of SLS in fabricating the larger size and lightweight SiC components.

4 Conclusions

The SiC composites have been fabricated by RMI of the porous C_f/SiC/C green bodies, which were obtained by the SLS process from the C_f and PR mixture with the addition of α-SiC particles. The initially introduced α-SiC particles play an important role in improving the flowability (AOR from 53° to 42°), reducing the porosity (from 74.89% to 67.29%), pore size (from 21.04 to 18.77 μm), and flexural strength (from 7.70 to 9.41 MPa) of the C_f/SiC/C green bodies. The SiC composites are mainly composed of typical SiC, residual Si, and residual C_f from partially siliconized C_f. Furthermore, the results indicate that the initial addition of SiC particles can not only avoid the formation of large-sized "silicon lakes" and improve the microstructural homogeneity, but also reduce the contents of residual silicon. More importantly, the β-SiC layer formed by RMI can act as a diffusion barrier to prevent the fibers from siliconization, and the residual C_f could improve the K_{IC} by fiber breakage. The maximum density of 2.749±0.006 g·cm^{-3} and K_{IC} of 3.30±0.06 MPa·m$^{1/2}$ are simultaneously achieved, and the medium flexural strength only possesses 250±11 MPa for the SiC composite sample with the addition of 15 vol% α-SiC particles. In addition, the α of the SiC composites is approximately 4.29×10^{-6} K^{-1} from RT to 900 ℃, and the κ at RT is in the range of 80.15–92.48 W·m^{-1}·K^{-1}, whose values decrease to 27.21–35.81 W·m^{-1}·K^{-1} at 900 ℃. Additionally, we reported the high-temperature mechanical properties of laser additive manufacturing SiC composites. The high-temperature strength (1200 ℃) of the SiC:IM = 0.20 sample increases to 287 MPa, which is 15% higher than the strength at RT. The fracture mode transition and crack healing contribute to strength improvement. Although the versatile performance still need to be further optimized, this study provides a new opportunity to fabricate the SiC composites.

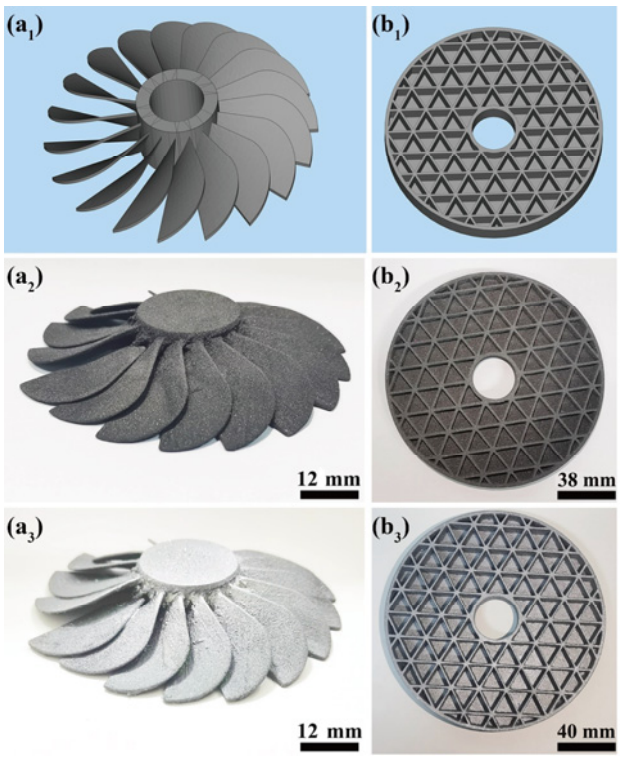

Fig. 16 C_f/SiC/C green bodies and sintered SiC composites with complex structures fabricated via SLS: (a_1–a_3) turbine blade; (b_1–b_3) flat mirror (the subscripts 1, 2, and 3 represent the STL models, printed C_f/SiC/C green bodies, and sintered SiC composites, respectively).

Acknowledgements

The authors would like to express sincere thanks to Prof. Jiang Li from Shanghai Institute of Ceramics, Chinese Academy of Sciences (CAS) for his constructive and very detailed suggestions on the improvement of the quality of this manuscript. This work was supported by the National Natural Science Foundation of China (Nos. 52073299, 52172077, U22A20129, and 51902329), the National Key R&D Program of China (No. 2022YFB3706303), and the Youth Innovation Promotion Association CAS (No. 2018289).

Declaration of competing interest

The authors have no competing interests to declare that are relevant to the content of this article.

References

[1] Xu YD, Cheng LF, Zhang LT. Carbon/silicon carbide composites prepared by chemical vapor infiltration combined with silicon melt infiltration. *Carbon* 1999, **37**: 1179–1187.

[2] Yang JH, Ai YJ, Lv XX, *et al*. Fabrication of C/C–SiC composites using high-char-yield resin. *Int J Appl Ceram Technol* 2021, **18**: 449–456.

[3] Liu GW, Zhang XZ, Yang J, *et al*. Recent advances in joining of SiC-based materials (monolithic SiC and SiC_f/SiC composites): Joining processes, joint strength, and interfacial behavior. *J Adv Ceram* 2019, **8**: 19–38.

[4] Huang XT, Chen SG, Sun HR, *et al*. Honeycomb sandwich structure of C_f/SiC ceramic matrix composites prepared by PIP–CVI. *Key Eng Mat* 2014, **602–603**: 422–425.

[5] Kim SY, Woo SK, Han IS, *et al*. The carbon black effect on crack formation during pyrolysis step in liquid silicon infiltration process for C_f/C–SiC composites. *J Ceram Soc Jan* 2010, **118**: 1075–1078.

[6] Wang CP, Tang J, Liu HL, *et al*. Preparation of C_f/SiC composites by liquid silicon infiltration. *Key Eng Mat* 2010, **434–435**: 103–105.

[7] Liang JJ, Xiao HN, Gao PZ, *et al*. Microstructure and properties of 2D-C_f/SiC composite fabricated by combination of CVI and PIP process with SiC particle as inert fillers. *Ceram Int* 2017, **43**: 1788–1794.

[8] Janssen R, Scheppokat S, Claussen N. Tailor-made ceramic-based components—Advantages by reactive processing and advanced shaping techniques. *J Eur Ceram Soc* 2008, **28**: 1369–1379.

[9] Li S, Zhang YM, Han JC, *et al*. Effect of carbon particle and carbon fiber on the microstructure and mechanical properties of short fiber reinforced reaction bonded silicon carbide composite. *J Eur Ceram Soc* 2013, **33**: 887–896.

[10] Chen ZW, Li ZY, Li JJ, *et al*. 3D printing of ceramics: A review. *J Eur Ceram Soc* 2019, **39**: 661–687.

[11] Hassanin H, Essa K, Elshaer A, *et al*. Micro-fabrication of ceramics: Additive manufacturing and conventional technologies. *J Adv Ceram* 2021, **10**: 1–27.

[12] Liu G, Zhang XF, Chen XL, *et al*. Additive manufacturing of structural materials. *Mat Sci Eng R* 2021, **145**: 100596.

[13] He RJ, Zhou NP, Zhang KQ, *et al*. Progress and challenges towards additive manufacturing of SiC ceramic. *J Adv Ceram* 2021, **10**: 637–674.

[14] Zou Y, Li CH, Tang YH, *et al*. Preform impregnation to optimize the properties and microstructure of RB-SiC prepared with laser sintering and reactive melt infiltration. *J Eur Ceram Soc* 2020, **40**: 5186–5195.

[15] Jin LZ, Zhang K, Xu TT, *et al*. The fabrication and mechanical properties of SiC/SiC composites prepared by SLS combined with PIP. *Ceram Int* 2018, **44**: 20992–20999.

[16] Xu TT, Cheng S, Jin LZ, *et al*. High-temperature flexural strength of SiC ceramics prepared by additive manufacturing. *Int J Appl Ceram Technol* 2020, **17**: 438–448.

[17] Zhu W, Fu H, Xu ZF, *et al*. Fabrication and characterization of carbon fiber reinforced SiC ceramic matrix composites based on 3D printing technology. *J Eur Ceram Soc* 2018, **38**: 4604–4613.

[18] Chen X, Yin J, Liu XJ, *et al*. Effect of laser power on mechanical properties of SiC composites rapidly fabricated by selective laser sintering and direct liquid silicon infiltration. *Ceram Int* 2022, **48**: 19123–19131.

[19] Lu J, Ni DW, Liao CJ, *et al*. Fabrication and microstructure evolution of C_{sf}/ZrB_2–SiC composites via direct ink writing and reactive melt infiltration. *J Adv Ceram* 2021, **10**: 1371–1380.

[20] Amirthan G, Udaya Kumar A, Balasubramanian M. Thermal conductivity studies on Si/SiC ceramic composites. *Ceram Int* 2011, **37**: 423–426.

[21] Zhang BH, Yin J, Wang YC, *et al*. Low temperature densification mechanism and properties of $Ta_{1-x}Hf_xC$ solid solutions with decarbonization and phase transition of Cr_3C_2. *J Materiomics* 2021, **7**: 672–682.

[22] Chen X, Yin J, Liu XJ, *et al*. Fabrication of core–shell chopped C_f-phenolic resin composite powder for laser additive manufacturing of C_f/SiC composites. *Polymers* 2021, **13**: 463.

[23] Tan JH, Wong WLE, Dalgarno KW. An overview of powder granulometry on feedstock and part performance in the selective laser melting process. *Addit Manuf* 2017, **18**: 228–255.

[24] Zegzulka J, Gelnar D, Jezerska L, *et al*. Characterization and flowability methods for metal powders. *Sci Rep* 2020, **10**: 21004.

[25] Shang XJ, Zhu YM, Li ZH. Surface modification of silicon carbide with silane coupling agent and hexadecyl iodiele. *Appl Surf Sci* 2017, **394**: 169–177.

[26] Yang Y, Gu DD, Dai DH, *et al*. Laser energy absorption behavior of powder particles using ray tracing method during selective laser melting additive manufacturing of aluminum alloy. *Mater Design* 2018, **143**: 12–19.

[27] Hozer L, Lee JR, Chiang YM. Reaction-infiltrated, net-shape SiC composites. *Mater Sci Eng* 1995, **195**: 131–143.

[28] Chen H, Wei QS, Zhang YJ, *et al*. Powder-spreading mechanisms in powder-bed-based additive manufacturing: Experiments and computational modeling. *Acta Mater* 2019, **179**: 158–171.

[29] Evans AG, Zok FW. The physics and mechanics of fibre-reinforced brittle matrix composites. *J Mater Sci* 1994, **29**: 3857–3896.

[30] Baxter RI, Rawlings RD, Iwashita N, *et al*. Effect of chemical vapor infiltration on erosion and thermal properties of porous carbon/carbon composite thermal insulation. *Carbon* 2000, **38**: 441–449.

[31] Ching WY, Xu YN, Rulis P, *et al*. The electronic structure

and spectroscopic properties of 3C, 2H, 4H, 6H, 15R and 21R polymorphs of SiC. *Mater Sci Eng* 2006, **422**: 147–156.

[32] Grewal G, Ankem S. Modeling matrix grain growth in the presence of growing second phase particles in two phase alloys. *Acta Metall Mater* 1990, **38**: 1607–1617.

[33] Hu J, Shi YN, Sauvage X, *et al*. Grain boundary stability governs hardening and softening in extremely fine nanograined metals. *Science* 2017, **355**: 1292–1296.

[34] Fu H, Zhu W, Xu ZF, *et al*. Effect of silicon addition on the microstructure, mechanical and thermal properties of C_f/SiC composite prepared via selective laser sintering. *J Alloys Compd* 2019, **792**: 1045–1053.

[35] Zhang H, Yang Y, Hu KH, *et al*. Stereolithography-based additive manufacturing of lightweight and high-strength C_f/SiC ceramics. *Addit Manuf* 2020, **34**: 101199.

[36] Watanabe H, Yamada N, Okaji M. Linear thermal expansion coefficient of silicon from 293 to 1000 K. *Int J Thermophys* 2004, **25**: 221–236.

[37] Li Z, Bradt RC. Thermal expansion and thermal expansion anisotropy of SiC polytypes. *J Am Ceram Soc* 1987, **70**: 445–448.

[38] Nakajo H, Utsumi Y. Thermal conductivity of pressureless-sintered SiC with B_4C and C. *Int J High Technol Ceram* 1986, **2**: 242–243.

[39] Liu DM, Lin BW. Thermal conductivity in hot-pressed silicon carbide. *Ceram Int* 1996, **22**: 407–414.

[40] Xia HY, Wang JP, Lin JP, *et al*. Thermal conductivity of SiC ceramic fabricated by liquid infiltrating molten Si into mesocarbon microbeads-based preform. *Mater Charact* 2013, **82**: 1–8.

[41] Huang QW, Zhu LH. High-temperature strength and toughness behaviors for reaction-bonded SiC ceramics below 1400 ℃. *Mater Lett* 2005, **59**: 1732–1735.

[42] Chen J, An QL, Ming WW, *et al*. Investigations on continuous-wave laser and pulsed laser induced controllable ablation of SiC_f/SiC composites. *J Eur Ceram Soc* 2021, **41**: 5835–5849.

[43] Ness JN, Page TF. Microstructural evolution in reaction-bonded silicon carbide. *J Mater Sci* 1986, **21**: 1377–1397.

[44] Dang XL, Zhao DL, Guo T, *et al*. Oxidation behaviors of carbon fiber reinforced multilayer SiC–Si_3N_4 matrix composites. *J Adv Ceram* 2022, **11**: 354–364.

[45] Wahl L, Lorenz M, Biggemann J, *et al*. Robocasting of reaction bonded silicon carbide structures. *J Eur Ceram Soc* 2019, **39**: 4520–4526.

[46] Tang J, Chang HT, Guo XT, *et al*. Preparation of carbon fiber-reinforced SiC ceramics by stereolithography and secondary silicon infiltration. *Ceram Int* 2022, **48**: 25159–25167.

[47] Lu ZL, Xia YL, Miao K, *et al*. Microstructure control of highly oriented short carbon fibres in SiC matrix composites fabricated by direct ink writing. *Ceram Int* 2019, **45**: 17262–17267.